

# Structural and proximity-induced ferromagnetic properties of topological insulator-magnetic insulator heterostructures

Zilong Jiang, Cui-Zu Chang, Chi Tang, Jian-Guo Zheng, Jagadeesh S. Moodera, and Jing Shi\*

Citation: [AIP Advances](#) **6**, 055809 (2016); doi: 10.1063/1.4943061

View online: <http://dx.doi.org/10.1063/1.4943061>

View Table of Contents: <http://aip.scitation.org/toc/adv/6/5>

Published by the [American Institute of Physics](#)

---

## Articles you may be interested in

[A comparative transport study of Bi<sub>2</sub>Se<sub>3</sub> and Bi<sub>2</sub>Se<sub>3</sub>/yttrium iron garnet](#)

[AIP Advances](#) **104**, 222409 (2014); 10.1063/1.4881975

[Magnetic modulation doping in topological insulators toward higher-temperature quantum anomalous Hall effect](#)

[AIP Advances](#) **107**, 182401 (2015); 10.1063/1.4935075

[Evidence for ferromagnetic coupling at the doped topological insulator/ferrimagnetic insulator interface](#)

[AIP Advances](#) **6**, 055813 (2016); 10.1063/1.4943157

---

# HAVE YOU HEARD?

Employers hiring scientists and  
engineers trust

**PHYSICS TODAY | JOBS**

[www.physicstoday.org/jobs](http://www.physicstoday.org/jobs)



# Structural and proximity-induced ferromagnetic properties of topological insulator-magnetic insulator heterostructures

Zilong Jiang,<sup>1</sup> Cui-Zu Chang,<sup>2</sup> Chi Tang,<sup>1</sup> Jian-Guo Zheng,<sup>3</sup>

Jagadeesh S. Moodera,<sup>2,4</sup> and Jing Shi<sup>1,a</sup>

<sup>1</sup>*Department of Physics and Astronomy, University of California, Riverside, CA 92521, USA*

<sup>2</sup>*Francis Bitter Magnetic Lab, Massachusetts Institute of Technology, Cambridge, MA 02139, USA*

<sup>3</sup>*Irvine Materials Research Institute, University of California, Irvine, CA 92697, USA*

<sup>4</sup>*Department of Physics, Massachusetts Institute of Technology, Cambridge, MA 02139, USA*

(Presented 12 January 2016; received 6 November 2015; accepted 4 December 2015; published online 25 February 2016)

The spontaneously broken time reversal symmetry can lead to the formation of an energy gap in the Dirac spectrum of the surface states of a topological insulator (TI) which can consequently give rise to a variety of interesting phenomena potentially useful for spintronics. In this work, we couple a non-magnetic TI to a high Curie temperature  $T_C$  magnetic insulator to induce strong exchange interaction via the proximity effect. We have successfully grown 5 quintuple layer thick ternary TI  $(\text{Bi}_x\text{Sb}_{1-x})_2\text{Te}_3$  films on atomically flat yttrium iron garnet (YIG) film with the combination of molecular beam epitaxy and pulsed laser deposition, in which the Fermi level position relative to the Dirac point is varied by controlling the Bi:Sb ratio. The anomalous Hall effect (AHE) and suppressed weak antilocalization (WAL) measured under out of plane magnetic fields reveal that the TI surface in contact with YIG is magnetized. Our high-quality  $(\text{Bi}_x\text{Sb}_{1-x})_2\text{Te}_3$ /YIG heterostructure provides a tunable system for exploring the quantum anomalous Hall effect (QAHE) at higher temperatures in TI-based spintronic devices. © 2016 Author(s). All article content, except where otherwise noted, is licensed under a Creative Commons Attribution 3.0 Unported License. [<http://dx.doi.org/10.1063/1.4943061>]

Breaking the time reversal symmetry (TRS) of a topological insulator (TI) opens up a mini-gap of the Dirac surface states and can lead to many interesting novel phenomena, such as the quantum anomalous Hall effect (QAHE),<sup>1</sup> topological magneto-electric effects,<sup>2</sup> and image magnetic monopoles.<sup>3</sup> The spontaneously broken TRS states are formed by introducing a ferromagnetic order in TI, which can usually be achieved with two experimental approaches: (1) random doping of transition metal elements (*i.e.* Fe, Mn, Cr or V), as successfully demonstrated in diluted magnetic semiconductors (DMS); (2) coupling the TI material with a magnetic insulator (MI) so that the surface states become ferromagnetic owing to the direct Heisenberg exchange interaction. In both cases, it is expected that an exchange gap opens up in the Dirac surface states. Obviously, doping a TI compound with transition metal atoms is a more straightforward and convenient way to reach the goal. Indeed, QAHE has been demonstrated in Cr- or V- doped  $(\text{Bi}_x\text{Sb}_{1-x})_2\text{Te}_3$  samples by several groups in the past three years.<sup>4-7</sup> In those materials, the QAHE phenomenon only occurs at temperatures two orders of magnitude smaller than the Curie temperature of the ferromagnetic transition. In randomly doped materials, not all spins are exchange coupled to form a uniform ferromagnetic phase. It is possible that non-uniformly distributed magnetic impurities play a role in preventing the QAHE state from appearing at higher temperatures.

<sup>a</sup>Corresponding author: [jing.shi@ucr.edu](mailto:jing.shi@ucr.edu)

To avoid random magnetic impurities, here we use a heterostructure consisting of a 3D TI and a magnetic insulator (MI), in which the broken TRS only occurs at the interface without disturbing the bulk states or causing any current shunting. More importantly, there are many available MIs with a wide range of transition temperatures, including ferrimagnets such as YIG ( $T_c \sim 550$  K),<sup>8</sup> ferromagnets such as EuS ( $T_c \sim 16.5$  K)<sup>9</sup> and EuO ( $\sim 77$  K),<sup>10</sup> and antiferromagnets such as BiFeO<sub>3</sub> ( $T_N \sim 640$  K),<sup>11</sup> which could offer a wide range of exchange coupling strength with TI. It is worth mentioning that commonly used ferromagnetic materials (Fe, Co and NiFe) are metallic and active, which are not suitable to form good heterostructures with TI. First, it is difficult to grow high quality metals on top of a TI due to intermixing between TI and metal atoms at the interface. As a result, deposition of ferromagnetic metals on TI can significantly alter the structure and physical properties of both TI and magnetic materials.<sup>12</sup> Second, the resistivity of TI compounds is usually one to two orders of magnitude larger than that of ferromagnetic metals. Therefore, the conduction is dominated by the adjacent metal layers.

In this work, we choose YIG, a MI with a large band gap ( $\sim 2.85$  eV) as an under-layer to form the heterostructure with  $(\text{Bi}_x\text{Sb}_{1-x})_2\text{Te}_3$  TI compounds. After a complex optimization of thin film heterojunction growth, we successfully demonstrate that high-quality 5 QL thick  $(\text{Bi}_x\text{Sb}_{1-x})_2\text{Te}_3$  films can be grown on atomically flat YIG substrates. The heterostructure of TI on YIG is characterized by various analytical techniques. With transport measurements, we confirm the proximity induced ferromagnetism at the TI surface, as revealed by the anomalous Hall effect (AHE). Furthermore, by varying Bi:Sb ratio in  $(\text{Bi}_x\text{Sb}_{1-x})_2\text{Te}_3$ /YIG heterostructures grown under the same condition, both longitudinal and AHE resistivities could be systematically tuned. Despite large changes in both longitudinal and AHE resistivities while the Bi:Sb ratio is varied, the AHE conductivity remains approximately constant, suggesting that the AHE conductivity is almost independent of the Fermi level position. A comparison of the weak-antilocalization effect (WAL) in 5 QL TI-YIG, 20 QL TI-YIG and pure TI samples indicates that magnetic scattering occurs at the TI/MI interface, which becomes more visible in thin samples with reduced bulk conduction.

The YIG under-layer is a  $\sim 20$  nm single crystal film epitaxially grown on (111) gadolinium gallium garnet (GGG) substrate at 700 °C in a pulsed laser deposition (PLD) system. In the layer-by-layer growth mode, film quality and thickness are monitored by the reflection high energy electron diffraction (RHEED) pattern and its intensity oscillations. Fig. 1(a) displays the RHEED

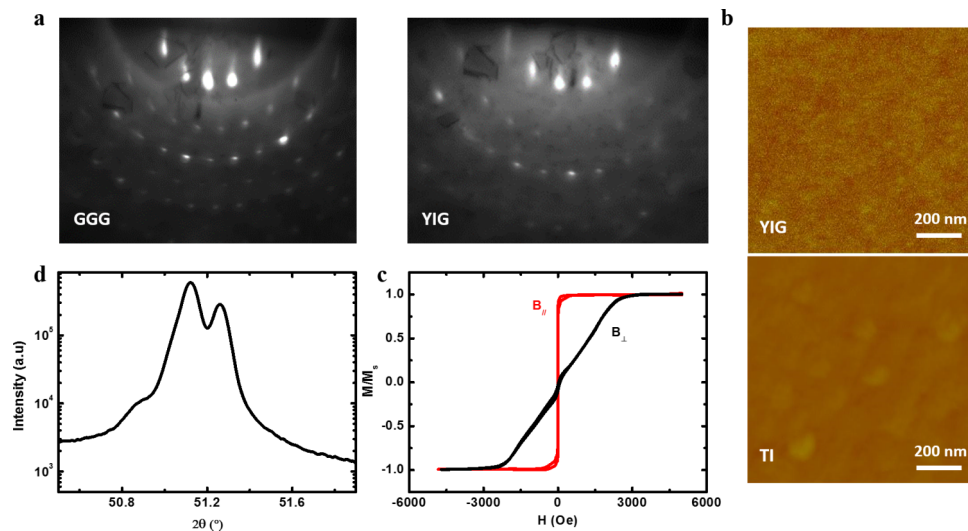


FIG. 1. Single crystal YIG film growth and characterization. (a) Epitaxial YIG (111) film grown on GGG as indicated by the clear RHEED patterns taken in the PLD chamber. (b) AFM image of a typical YIG (111) sample with the rms roughness  $\sim 0.15$  nm and TI film grown on YIG with roughness less than 0.4 nm. (c) VSM data of YIG (111) sample shows a well-defined in-plane anisotropy. The out-of-plane curve indicates a saturation field around 2500 Oe which slightly varies in different YIG samples. (d) XRD spectrum of YIG/GGG (111) sample. The (444) diffraction peak is clearly visible.

patterns taken before and after the YIG deposition. The consistency in the RHEED pattern strongly suggests the epitaxial growth of YIG film on the GGG (111) substrate. The post-growth annealing is performed in a separate furnace with oxygen flow, which is found to be favorable for smoother surface and larger magnetization. Atomic force microscopy (AFM) image of a typical  $\sim 20$  nm YIG film is presented in Fig. 1(b), indicating a rms roughness of  $\sim 0.15$  nm over a  $1 \mu\text{m} \times 1 \mu\text{m}$  scan region. The extremely flat YIG surface is very favorable for constructing the heterostructures with thin TI films. Magnetization measurements with the magnetic field oriented in-plane and out-of-plane are taken with a vibrating sample magnetometer (VSM) at room temperature. VSM data of a representative YIG film is shown in Fig. 1(c), suggesting well-defined in-plane magnetic anisotropy. The in-plane magnetic hysteresis loop shows a coercive field  $\sim 2$  Oe and the out-of-plane saturation field is located  $\sim 2500$  Oe. X-ray diffraction (XRD) results shown in Fig. 1(d) further confirm that YIG has an epitaxial relation with the GGG substrate in the (111) growth direction and no other phases are observed. These results indicate that our YIG film is of single crystal-line quality and has atomically flat surface, which is important for preparing high-quality TI/MI heterostructures.

To form TI/MI heterostructures, atomic flat YIG (111) films are transferred to a ultra-high vacuum ( $< 5 \times 10^{-10}$  Torr) molecular beam epitaxy (MBE) chamber for  $(\text{Bi}_x\text{Sb}_{1-x})_2\text{Te}_3$  TI compounds growth. In-situ high temperature annealing ( $600^\circ\text{C}$ , 60 mins) is performed for degassing prior to growth. As shown in Fig. 2(a), the RHEED pattern is taken again in the MBE chamber to ensure the same excellent quality of YIG surface condition. The clear and well-defined RHEED pattern of YIG indeed excludes the possibility of sample degradation during transfer or annealing process. 5 QL  $(\text{Bi}_x\text{Sb}_{1-x})_2\text{Te}_3$  film is then deposited on the YIG (111) substrate at  $230^\circ\text{C}$ . For comparison, 20 QL  $\text{Bi}_2\text{Se}_3$ /YIG and  $\text{Bi}_2\text{Se}_3$ /Si are grown using the same procedures. Fig. 2(a) (right panel) is the in-situ RHEED pattern right after the TI growth. The sharp and streaky diffraction spots indicate a very flat surface and high quality crystalline TI film grown on YIG (111) substrate. Before it is taken out of the MBE chamber, the heterostructure sample is usually capped with a 5 QL epitaxial Te film on top as a passivation layer.

High single crystal quality  $(\text{Bi}_x\text{Sb}_{1-x})_2\text{Te}_3$  thin film on YIG substrate is further verified by XRD on a 20 QL TI/YIG/GGG sample (Fig. 2(b)). The TI layer shows the (00 $l$ ) type reflections along the growth direction and the Bragg peak positions of the TI layer on YIG agree very well with the reference. Except for the YIG/GGG (444) peak or the (001) peak of Te capping layer, no impurity phase is present. Strong Kiessig fringes are visible around the TI's (003) diffraction peak (not shown), indicating good  $(\text{Bi}_x\text{Sb}_{1-x})_2\text{Te}_3$  surface and  $(\text{Bi}_x\text{Sb}_{1-x})_2\text{Te}_3$ /YIG (111) interface correlation. Fig. 2(d) shows a typical cross-sectional high resolution transmission electron microscopy (HRTEM) image of 5 QL TI/YIG sample. The HRTEM image confirms that  $(\text{Bi}_x\text{Sb}_{1-x})_2\text{Te}_3$  thin film grown on YIG maintains a good layered structure and the interface between TI and YIG is reasonably clean and sharp. The HRTEM image also supports the conclusion drawn from XRD data: YIG is a single crystal with the same orientation as that of GGG, the TI is grown along the  $c$  axis on the (111) surface of YIG and Te protection layer has an epitaxial relation with  $(\text{Bi}_x\text{Sb}_{1-x})_2\text{Te}_3$  film.

As schematically depicted in Fig. 3(a), for transport studies, the heterostructure sample TI/YIG is patterned into Hall bar structures (channel width of  $100 \mu\text{m}$  and length of  $900 \mu\text{m}$ ) by standard photolithography and etched by the inductively coupled plasma. The Au/Ti contacts are deposited with an electron-beam evaporator. The four-terminal electrical transport measurements are taken in a Physical Property Measurement System over a wide range of temperatures down to 2 K and under perpendicular magnetic fields up to 14 T. It is noted that the YIG substrate layer is found to remain highly insulating ( $> 40 \text{ G}\Omega$ ) after the TI film etch and device fabrication. Hence, the transport signal in TI/MI heterostructures originates from the TI without any contribution from possible shunting by the surface of YIG.

Fig. 3(b) displays the temperature dependent  $R_{xx}$  of TI/YIG samples. In this work, we include three  $(\text{Bi}_x\text{Sb}_{1-x})_2\text{Te}_3$ /YIG heterostructure samples with different Bi fractions for investigation:  $\text{Bi}_2\text{Te}_3$ /YIG ( $x=1$ ),  $(\text{Bi}_{0.36}\text{Sb}_{0.64})_2\text{Te}_3$ /YIG ( $x=0.36$ ) and  $(\text{Bi}_{0.24}\text{Sb}_{0.76})_2\text{Te}_3$ /YIG ( $x=0.24$ ). It is known from previous studies<sup>13</sup> that as  $x$  is varied, the Fermi level position of  $(\text{Bi}_x\text{Sb}_{1-x})_2\text{Te}_3$  is systematically tuned, so is the carrier concentration. This Fermi level position control via the doping

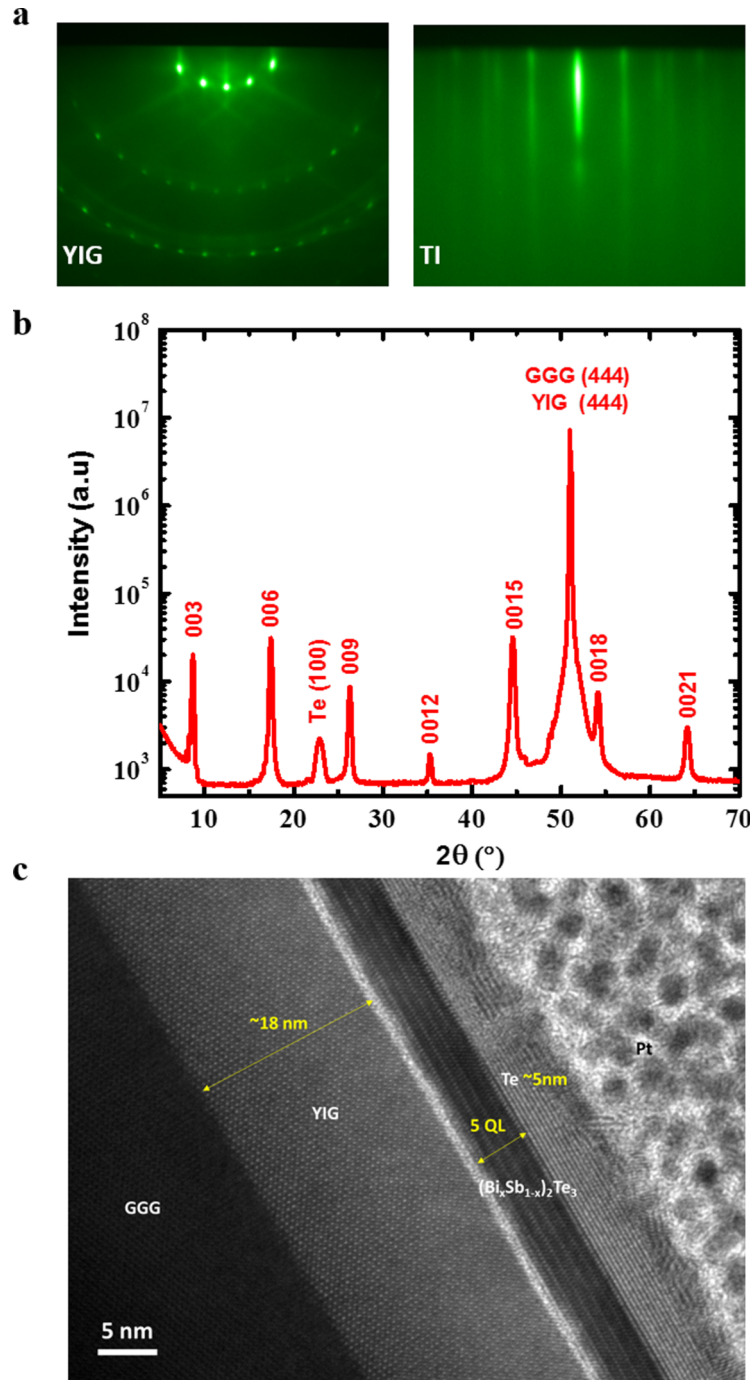


FIG. 2. Structural properties of TI/YIG samples. (a) RHEED patterns taken before and right after TI growth in the MBE chamber, indicating high crystalline quality of TI film on YIG (111). (b) XRD spectrum of a representative 20 QL TI/YIG/GGG (111) sample. (c) HRTEM image of 5 QL  $(\text{Bi}_x\text{Sb}_{1-x})_2\text{Te}_3$ /YIG/GGG heterostructure.

level in  $(\text{Bi}_x\text{Sb}_{1-x})_2\text{Te}_3$ /YIG allows us to probe the relative contribution to the electrical transport from the bulk and surface states. In Fig. 3(b), the resistance of  $\text{Bi}_2\text{Te}_3$  (red curve) is much lower than that of the other two samples and shows a metallic behavior over the whole temperature range (300 K to 2 K). For the  $x=0.36$  sample,  $R_{xx}$  increases and has a weak insulating behavior as the temperature is decreased. However, for the  $x=0.24$  sample, the resistance behavior is strongly insulating. The different behaviors in the temperature dependence along with the carrier concentration



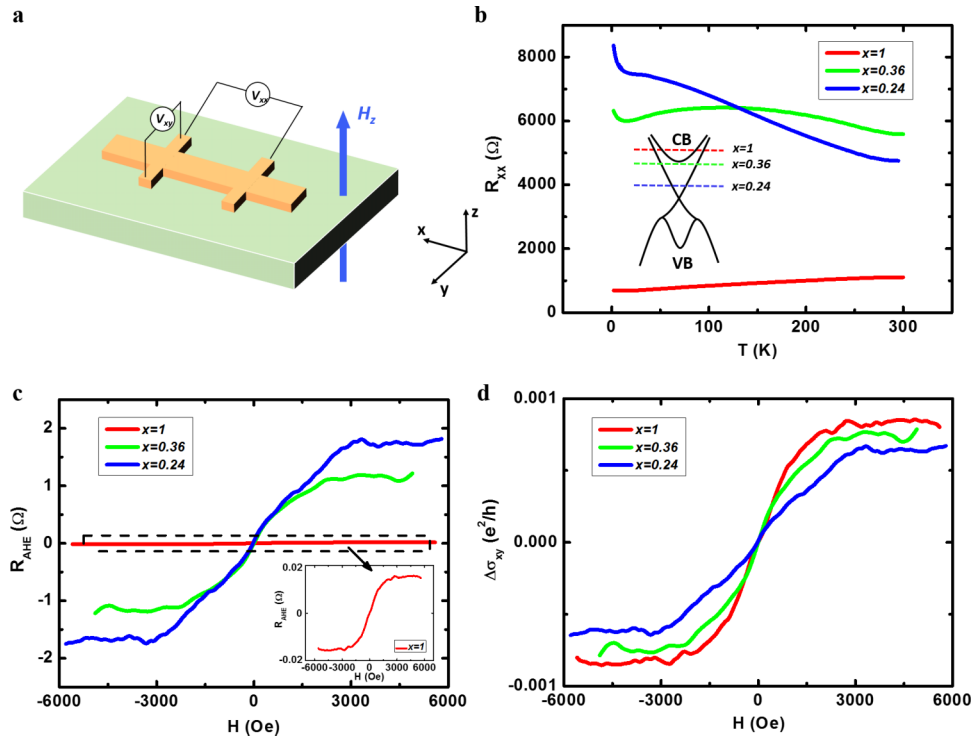


FIG. 3. Proximity induced anomalous Hall effect in 5 QL  $(\text{Bi}_x\text{Sb}_{1-x})_2\text{Te}_3/\text{YIG}$  heterostructures. (a) Schematic illustration of TI/YIG device for transport measurements. (b) Temperature dependence of  $R_{xx}$  in  $(\text{Bi}_x\text{Sb}_{1-x})_2\text{Te}_3/\text{YIG}$  samples with different Bi fractions. The inset shows schematics of electronic band structure of  $(\text{Bi}_x\text{Sb}_{1-x})_2\text{Te}_3$ , indicating the shift of the Fermi energy as  $x$  is varied. (c) The observation of anomalous Hall effect in  $(\text{Bi}_x\text{Sb}_{1-x})_2\text{Te}_3/\text{YIG}$  samples at different Bi fractions. The inset shows the anomalous Hall signal for  $\text{Bi}_2\text{Te}_3/\text{YIG}$  sample on a significant reduced scale. (d) Field-dependent anomalous Hall conductance in  $(\text{Bi}_x\text{Sb}_{1-x})_2\text{Te}_3/\text{YIG}$  when  $x$  is varied.

results obtained from the ordinary Hall data (not shown) indicate that the Fermi level shifts from the conduction band to the band gap with a depletion of bulk carriers when  $x$  decreases from 1 to 0.24. Fig. 3(b) inset shows a schematic illustration of the band diagram for  $(\text{Bi}_x\text{Sb}_{1-x})_2\text{Te}_3$  with different Fermi energies. The relative Fermi level positions at different Bi fractions are inferred from Hall carrier densities.

The proximity induced ferromagnetism is identified by the observation of the AHE in  $(\text{Bi}_x\text{Sb}_{1-x})_2\text{Te}_3/\text{YIG}$  samples. Fig. 3(c) shows the nonlinear contribution to the total Hall data in three  $(\text{Bi}_x\text{Sb}_{1-x})_2\text{Te}_3/\text{YIG}$  heterostructure samples with various Bi fractions, after the linear ordinary Hall background is removed. The shape of the nonlinear Hall signal in  $(\text{Bi}_x\text{Sb}_{1-x})_2\text{Te}_3/\text{YIG}$  samples resembles that of the YIG out-of-plane hysteresis loop, although the saturation field varies slightly possibly due to the variation of the growth induced anisotropy of YIG films. Additional evidence and discussions could be found in Ref. 14. Hence, the nonlinear Hall signal originates from AHE, as a consequence of the induced ferromagnetic surface of the topological insulator in contact with YIG.<sup>15</sup> Such an AHE signal corresponds to the short-range magnetic proximity effect on the bottom metallic surface of TI film. More importantly, the AHE resistance exhibits a distinct difference in magnitude as shown in Fig. 3(c). The inset of Fig. 3(c) is the AHE curve for  $\text{Bi}_2\text{Te}_3/\text{YIG}$  sample on a much smaller scale. The  $R_{AHE}$  for  $x=0.24$  sample shows a two-orders-of-magnitude enhancement compared with  $\text{Bi}_2\text{Te}_3/\text{YIG}$ , indicating that the more insulating sample (surface dominated) has larger AHE resistance. To further probe the relation between the ferromagnetic property (AHE) and electrical resistivity of TI/YIG samples, we calculate the AHE conductivity  $\sigma_{xy} = \frac{\rho_{xy}}{\rho_{xx}^2 + \rho_{xy}^2}$  and plot it as a function of magnetic field for different Bi fractions. As displayed in Fig. 3(d), it is interesting that although both  $R_{AHE}$  and  $R_{xx}$  exhibit a strong dependence on  $x$ ,  $\sigma_{xy}$  is almost constant. In our samples, the Fermi level position relative to the Dirac point is varied by doping or  $x$ . Thus, the

doping is a knob which controls both  $R_{xx}$  in Fig. 3(b) and the corresponding  $R_{AHE}$  in Fig. 3(c). However, it is found that the anomalous Hall conductivity is relatively insensitive to the Fermi level of  $(\text{Bi}_x\text{Sb}_{1-x})_2\text{Te}_3/\text{YIG}$  system.

The electrons in topological surface states on the Dirac cone could acquire the  $\pi$  Berry phase, which results in a destructive interference and consequently leads to the WAL effect which has been observed in most TI materials. Nevertheless, this  $\pi$  Berry phase is vulnerable to spin-dependent scattering which breaks the TRS, *i.e.* the exchange interaction with magnetic add-layer on the topological surface (Fig. 4(a)).<sup>16,17</sup> As a result, the suppression of WAL effect is expected from magnetic scattering at the interface between TI and YIG. Fig. 4(b) shows the low-field magneto-conductance (MC) data of three 5 QL  $(\text{Bi}_x\text{Sb}_{1-x})_2\text{Te}_3/\text{YIG}$  samples and two reference samples: 20 QL  $\text{Bi}_2\text{Se}_3/\text{YIG}$  and  $\text{Bi}_2\text{Se}_3/\text{Si}$ . The MC data of pure  $\text{Bi}_2\text{Se}_3$  on Si can be fitted very well by the Hikami-Larkin-Nagaoka formula<sup>18</sup> with the pre-factor indicating strong WAL signal for single coherent channel, consistent with the results of pure TI samples reported by other groups.<sup>19–21</sup> However, a clear WAL suppression is observed in 20 QL  $\text{Bi}_2\text{Se}_3/\text{YIG}$ . Since YIG is grown at  $\sim 700^\circ\text{C}$  while TI is grown at  $\sim 250^\circ\text{C}$  later, we do not expect any significant diffusion of Fe atoms to dope the TI to form the magnetic scattering center. Hence, the WAL suppression in TI/YIG heterostructure is a phenomena owing to the magnetic scattering strictly at the TI/MI interface, which is different from that in the Cr-doped TI<sup>22</sup> or Fe/TI sample.<sup>23</sup> Furthermore, a stronger magnetic proximity effect should occur in same heterostructure samples but with a thinner and more insulating TI layer. As also shown in Fig. 4(b), the cusp-like MC signal is almost quenched in 5 QL  $(\text{Bi}_x\text{Sb}_{1-x})_2\text{Te}_3/\text{YIG}$  samples, which are more bulk insulating. The dramatic change of the WAL effect in TI/YIG samples not only reveals its origin from the 2D topological surface states, also confirms the effect of the magnetic scattering at the TI/MI interface.<sup>24</sup>

In summary, the proximity induced ferromagnetism in TI/YIG samples has been investigated via the AHE and the suppression of the WAL effect in high-quality 5 QL  $(\text{Bi}_x\text{Sb}_{1-x})_2\text{Te}_3/\text{YIG}$  heterostructures. The most important advantage of such a system is that the TRS breaking happens at the interface between TI and MI without altering bulk states or introducing defects. More efforts will be made to further enhance the exchange coupling between TI and MI by improving the interface quality. A stronger exchange interaction will generate a larger topological gap on the TI surface, leading to the observation of QAHE at higher temperatures.

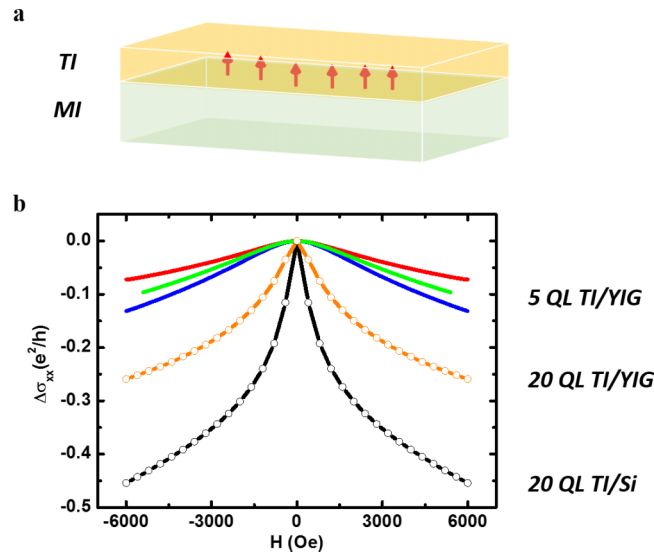


FIG. 4. The suppression of weak-antilocalization effect in TI/YIG heterostructures. (a) Schematic illustration of ferromagnetic exchange coupling at the interface between TI and MI. (b) Field-dependent magneto-conductance data for TI/YIG and TI/Si samples. The black circles indicate a strong WAL effect in TI/Si sample. The WAL signal is suppressed in 20 QL TI/YIG (orange circles), and almost quenched in 5 QL TI/YIG heterostructure samples, revealing the effect of the magnetic scattering caused by adjacent magnetic layer.

## ACKNOWLEDGEMENTS

The authors would like to thank V. Aji and P. Wei for fruitful discussions, and W. Beyermann, D. Humphrey, M. Aldosary, B. Yang & R. Zheng for the technical assistance. YIG growth, device fabrication, measurements of magnetic and transport properties at UCR were supported as part of the SHINES, an Energy Frontier Research Center funded by the U.S. Department of Energy, Office of Science, Basic Energy Sciences under Award # SC0012670. TI growth and x-ray diffraction were performed at MIT and supported by the STC Center for Integrated Quantum Materials under NSF Grant No. DMR-1231319, NSF DMR Grants No. 1207469 and ONR Grant No. N00014-13-1-0301. The TEM specimen preparation and HRTEM work was carried out at Irvine Materials Research Institute at UC Irvine, using instrumentation funded in part by the National Science Foundation Center for Chemistry at the Space-Time Limit (CHE-082913).

- <sup>1</sup> R. Yu, W. Zhang, H.-J. Zhang, S.-C. Zhang, X. Dai, and Z. Fang, *Science* **329**, 61 (2010).
- <sup>2</sup> A. M. Essin, J. E. Moore, and D. Vanderbilt, *Phys. Rev. Lett.* **102**, 146805 (2009).
- <sup>3</sup> X.-L. Qi, R. Li, J. Zang, and S.-C. Zhang, *Science* **323**, 1184 (2009).
- <sup>4</sup> C.-Z. Chang, J. Zhang, X. Feng, J. Shen, Z. Zhang, M. Guo, K. Li, Y. Qu, P. Wei, L.-L. Wang, Z. Ji, Y. Feng, S. Ji, X. Chen, J. Jia, X. Dai, Z. Fang, S.-C. Zhang, K. He, Y. Wang, L. Lu, X. Ma, and Q.-K. Xue, *Science* **340**, 167 (2013).
- <sup>5</sup> J. G. Checkelsky, R. Yoshimi, A. Tsukazaki, K.S. Takahashi, Y. Kozuka, J. Falson, M. Kawasaki, and Y. Tokura, *Nature Physics* **10**, 731 (2014).
- <sup>6</sup> X. Kou, S. Guo, Y. Fan, L. Pan, M. Lang, Y. Jiang, Q. Shao, T. Nie, K. Murata, J. Tang, Y. Wang, L. He, T. Lee, W. Lee, and K.-L. Wang, *Phys. Rev. Lett.* **113**, 137201 (2014).
- <sup>7</sup> C.-Z. Chang, W. Zhao, D. Y. Kim, H. J. Zhang, B. A. Assaf, D. Heiman, S. C. Zhang, C. X. Liu, M. H. W. Chan, and J. S. Moodera, *Nat. Mat.* **14**, 473-477 (2015).
- <sup>8</sup> Z. Jiang, F. Katmis, C. Tang, P. Wei, J. S. Moodera, and J. Shi, *Appl. Phys. Lett.* **104**, 222409 (2014).
- <sup>9</sup> P. Wei, F. Katmis, B. A. Assaf, H. Steinberg, P. JarilloHerrero, D. Heiman, and J. S. Moodera, *Phys. Rev. Lett.* **110**, 186807 (2013).
- <sup>10</sup> A. Swartz, P. Odenthal, Y. Hao, R. Ruoff, and R.K. Kawakami, *ACS Nano* **6**, 10063 (2012).
- <sup>11</sup> W. Yang, S. Yang, Q. Zhang, Y. Xu, S. Shen, J. Liao, J. Teng, C. Nan, L. Gu, Y. Sun, K. Wu, and Y. Li, *Appl. Phys. Lett.* **105**, 222409 (2014).
- <sup>12</sup> J. Li, Z. Wang, A. Tan, P. Glans, E. Arenholz, C. Hwang, J. Shi, and Z. Qiu, *Phys. Rev. B* **86**, 054430 (2012).
- <sup>13</sup> J. Zhang, C. Z. Chang, Z. Zhang, J. Wen, X. Feng, K. Li, M. Liu, K. He, L. Wang, X. Chen, Q. Xue, X. Ma, and Y. Wang, *Nat. Commun.* **2**, 574 (2011).
- <sup>14</sup> Z. Jiang, C. Z. Chang, C. Tang, P. Wei, J. S. Moodera, and J. Shi, *Nano Lett.* **15**, 5835 (2015).
- <sup>15</sup> N. Nagaosa, J. Sinova, S. Onoda, A. H. MacDonald, and N. P. Ong, *Rev. Mod. Phys.* **82**, 1539-1592 (2010).
- <sup>16</sup> H.-Z. Lu, J.-R. Shi, and S.-Q. Shen, *Phys. Rev. Lett.* **107**, 076801 (2011).
- <sup>17</sup> X.-L. Qi, T. L. Hughes, and S.-C. Zhang, *Phys. Rev. B* **78**, 195424 (2008).
- <sup>18</sup> S. Hikami, A. Larkin, and Y. Nagaoka, *Prog.Theor.Phys.* **63**, 707 (1980).
- <sup>19</sup> A. A. Taskin, S. Sasaki, K. Segawa, and Y. Ando, *Phys. Rev. Lett.* **109**, 066803 (2012).
- <sup>20</sup> J. Chen, X. Y. He, K. H. Wu, Z. Q. Ji, L. Lu, J. R. Shi, J. H. Smet, and Y. Q. Li, *Phys. Rev. B* **83**, 241304(R) (2011).
- <sup>21</sup> L. Bao, L. He, N. Meyer, X. Kou, P. Zhang, Z. Chen, A.V. Fedorov, J. Zou, T.M. Riedemann, T.A. Lograsso, K.L. Wang, G. Tuttle, and F. Xiu, *Sci. Rep.* **2**, 726 (2012).
- <sup>22</sup> M. Liu, J. Zhang, C.-Z. Chang, Z. Zhang, X. Feng, K. Li, K. He, L.-L. Wang, X. Chen, X. Dai, Z. Fang, Q.-K. Xue, X. Ma, and Y. Wang, *Phys. Rev. Lett.* **108**, 036805 (2012).
- <sup>23</sup> H.-T. He, G. Wang, T. Zhang, I.-K. Sou, G. K.L. Wang, and J.-N. Wang, *Phys. Rev. Lett.* **106**, 166805 (2011).
- <sup>24</sup> C. Z. Chang, P. Wei, and J. S. Moodera, *Materials Research Society Bulletin* **39**, 867 (2014).